

# An Artificial Neural Network (ANN) based Aerothermal Optimization of Film Cooling Hole Locations on the Squealer Tip of an HP Turbine Blade

F. Yıldız<sup>a</sup>, E. Alpman<sup>b</sup>, L. Kavurmacıoğlu<sup>a</sup>, C. Camci<sup>c</sup>

<sup>a</sup>*Istanbul Technical University, Dept. of Mechanical Eng., 34437 Istanbul, Turkey*

<sup>b</sup>*Marmara University, Mechanical Eng. Dept., Göztepe Campus, 34722 Istanbul, Turkey*

<sup>c</sup>*The Pennsylvania State University, Dept. of Aerospace Engineering Turbomachinery Aero-Heat Transfer Lab, University Park, PA, 16802, USA*

---

## Abstract

In this study, positions of film cooling holes at the squealer tip surface of a gas turbine blade are optimized for cooling effectiveness and aerodynamic performance. A computational cascade flow model including aerodynamic and heat transfer validation is employed for aero-heat transfer multiobjective optimization purposes. The computational study modeled the turbulent flow environment using the two-equation SST  $k-\omega$  model. Five film cooling holes are used with a blowing ratio equal to 1 and 0.4. The positions of four film cooling holes along the y-direction are used as input parameters of optimization. Specific utilities of the RANS-based open-source computational fluid dynamics software OpenFOAM® are used to change film cooling hole locations without modifying the computational grid. Multiobjective optimization is performed using an algorithm with an artificial neural network for fast fitness function predictions. A 0.31% drop in aerodynamic loss and a 12.95% reduction in heat transfer coefficient is obtained for the optimized case. The heat transfer rate on the cavity surface of the best film cooling case is 7.2% better than the worst case. After the optimization process, the low blowing ratio and casing relative motion effects are studied in three cases. While a low blowing ratio has not much impact on aerodynamic performance, casing relative motion improves it by almost 8%. On the other hand, a reduction in blowing ratio to 0.4 increases the magnitude of heat transfer on the tip region by 4-7%, while the addition of casing relative motion decreases it by about 9-12%. The impact of casing relative motion is more dominant than the impact of blowing ratio for the heat transfer on the tip surface.

**Keywords:** Film cooling, Squealer blade tip, Blowing ratio, Casing relative motion, Multiobjective optimization

---

## 1. Introduction

The thermal efficiency of gas turbine engines has become increasingly critical over the years for better fuel efficiency and improved specific power. Temperatures of the first stage turbine inlets easily exceed 1300 °C [1]. High thermal loads occur on turbine blades and create durability problems. As a result, the cooling of turbine

blades

becomes a must, and film cooling is the preferred external cooling method for a turbine blade.

## Nomenclature

### Latin Symbols

$\Delta C_{p0}$	Total pressure loss coefficient
$\hat{Y}_i$	Network predictions
$C$	Chord
$C_{p0}$	Total pressure coefficient
$C_p$	Static pressure coefficient
$C_p$	Specific heat capacity
$C_x$	Axial chord
$d$	Film cooling hole diameter
$h$	Blade span
$h$	Convective heat transfer coefficient
$M$	Blowing ratio
$p$	Pressure
$p_0$	Mass averaged total pressure at the inlet
$p_{0i}$	Total pressure
$p_i$	Mass averaged pressure at the inlet
$Pr$	Laminar Prandtl number
$Pr_t$	Turbulent Prandtl number
$q''_w$	Wall heat flux
$S$	Blade pitch
$s$	Squealer height
$T$	Temperature
$t$	Tip clearance
$U_\infty$	Mainstream velocity
$U_c$	Coolant velocity
$U_i$	Inlet velocity
$U_m$	Mean blade velocity at mid-span of AFTRF test blade
$w$	Squealer width

$Y_i$

Actual testing data

### Greek Symbols

$\alpha$	Inlet flow angle
$\delta C_p$	Uncertainty of static pressure coefficient
$\delta h$	Uncertainty of heat transfer coefficient
$\kappa_{eff}$	Effective heat conductivity
$\kappa_t$	Turbulent heat conductivity
$\nu$	Kinematic viscosity
$\nu_t$	Turbulent viscosity
$\rho$	Density
$\rho_\infty$	Mainstream density
$\rho_c$	Coolant density
$\omega$	Specific rate of dissipation

### Abbreviations

AFTRF	Axial flow turbine research facility
ANN	Artificial neural network
CFD	Computational fluid dynamics
FC	Film cooling
FFNN	Feedforward neural network
MSE	Mean square error
NSGA – II	Nondominated sorting genetic algorithm
PS	Pressure side
RANS	Reynolds-averaged Navier-Stokes
SS	Suction side
SST	Shear stress transport

Unlike internal cooling, external cooling decreases the convective heat transfer rate to protect the blade surface from melting and local oxidation damage.

Especially for unshrouded blades, cooling of blade tip becomes more difficult with leakage flow that occurs with pressure difference and accelerates from the suction side (SS) to the pressure side (PS). This leakage has critical importance for aerodynamic efficiency and cooling of the blade tip. Thus, many studies focus on tip designs and film cooling to protect the turbine blade's tip region, decreasing leakage flow and convective heat transfer rate.

The rate of tip leakage loss is related to many different parameters. Gap height between tip surface and stationary shroud is one of them, and tip leakage flow decreases with decreasing gap height because of the viscosity effect. Saha et al. [2] have mentioned that tip gap height can be reduced using a squealer tip design. A squealer tip design allows an uninterrupted turbine operation in a potential rubbing incident between a blade and the casing. The only damage is generally to the squealer cavity rims, and the tip cooling system remains intact. In addition to this, a separation vortex occurs near the pressure side rim of the squealer tip and creates resistance to leakage loss. It acts as a labyrinth seal, and Azad et al. [3] have investigated this subject. Tip clearance also affects cooling performance on the tip region as leakage mass flow rate varies. Acharya et al. [4] showed that film cooling effectiveness increases with decreasing clearance as leakage mass flow is reduced.

Altering the conventional tip platform design could significantly reduce tip leakage loss. The squealer tip design is one of the most popular strategies to date. Key and Arts [5] studied a squealer tip and showed that their squealer tip design significantly reduced tip leakage when compared to a flat tip. Like this research, Schabowski et al. [6] have compared winglet and plane tip designs and reported that winglet tip decreases aerodynamic loss. Dey and Camci [7] also studied several winglet tip designs in the rotating turbine rig, Axial Flow Turbine Research Facility (AFTRF). They compared PS and SS tip extensions against a baseline tip and showed that PS tip extension played a significant role in decreasing tip leakage loss. Ledezma et al. [8] have investigated the impact of different tip designs on tip leakage flow. They showed a squealer tip design without a pressure side rim, and a pressure side winglet design has higher total exit pressure than the conventional squealer tip design.

Besides increasing aerodynamic performance, tip desensitization decreases the heat transfer rate at the tip surface because of tip leakage flow's reduced mass flow rate. Yan et al. [9] investigated the influences of winglet and squealer tips on heat transfer and leakage loss. Besides, the impact of the multi-cavity tip on the aerothermal performance of turbine blades has been studied by Du et al. [10]. They showed that the single-cavity tip offers better performance than their divided multi-cavity tip design and plane tip case. Jiang et al. [11] researched the

impact of squealer tip design with winglets on turbine aerothermal performance using three different tip designs. They demonstrated performance improvements when compared to conventional squealer tip design. Unlike these investigations, Zhou et al. [12] presented that blade tip coolant injection could effectively reduce cavity floor heat load. However, its effect on the casing is less pronounced. They also showed that simultaneous tip film cooling and casing purge cooling could effectively reduce the casing and cavity floor's heat load.

Film cooling can also change the tip flow characteristic at the tip gap. Complex viscous flow in the tip gap is highly critical, especially for aerodynamically optimized tip designs. Wang et al. [13] have shown that leakage flow near the leading-edge decreases with film cooling compared to without a film cooling case. Sakaoglu and Kahveci [14] investigated the combined effects of film cooling and rotation on tip gap flow characteristics. They reported that the heat transfer is reduced on the tip surface with the effect of rotation for both cooled and uncooled cases and rotation also presses the high heat transfer zone to the pressure side of the cavity. They also showed the impact of cavity depth on the film cooling performance. They pointed out that increasing the cavity depth reduces the average heat transfer coefficient above the depth-to-width ratio of 1.5. The impact of rotation was also investigated using casing relative motion in this study. The heat transfer reduction in the tip region and pushing high heat transfer zone to the pressure side rim of the cavity surface were also investigated..

Tip leakage flow contains vortices and has a complex structure that tries to pull up the film cooling layer from the tip surface. In this situation, film cooling cannot effectively protect the tip surface. The solution to this problem is to use angled and shaped film cooling holes. Eriksen and Goldstein [15] investigated the impact of using various angled film cooling holes and presented that 35° angled film cooling holes show better cooling performance than a normal injection. Yan et al. [16] also researched that subject with different injection angles in pitchwise and streamwise directions. They pointed out that for better film cooling performance, the pitchwise injection angle should be less than 30°, and the streamwise injection angle should be about 120°.

On the other hand, Kim and Metzger [17] studied slot-shaped film cooling holes close to the pressure side of the tip region. They reported a good performance, especially for the spanwise direction where the holes were located. However, this study selected cylindrical holes in the normal direction to understand the effect of hole position on heat transfer.

The blowing ratio is another crucial variable that changes cooling performance because coolant flow should have enough energy to surpass tip flow and create a proper coolant layer on the tip surface. Many studies focused on this subject and showed that increasing the blowing ratio increases the cooling performance [18, 19, 20] up to a specific value. Over that optimal value, the film cooling jet penetrates the free stream, and it starts to lose

its cooling effectiveness. An unnecessarily high blowing ratio also reduces the turbine efficiency by consuming too much pressurized air from the cycle. The blowing rate was selected equal to one throughout this optimization approach. On the other hand, after the optimization process, the impact of the blowing ratio in heat transfer and aerodynamic loss is studied with a blowing ratio equal to 0.4 for the best cooled three cases.

In addition to hole shape, injection angle, and blowing rate, the number and positions of holes significantly affect film cooling effectiveness and tip leakage flow characteristics. Rao and Camci [21] presented a tip injection study in the rotating turbine research rig (AFTRF). They observed that different injection locations have a measurable impact on the development of leakage vortex. Phase-locked and time-accurate total pressure surveys obtained downstream of the rotor of the AFTRF documented the impact of the tip cooling injection on the tip leakage flow structure. Cheng et al. [22] studied camber line and suction side holes with changing numbers and showed that film cooling protection increased with an increasing number of holes, and cooling of the blade tip leading edge was more challenging than in the other zones. Another numerical study of different film hole arrangements was reported by Yang et al. [23]. They used three different hole arrangements. The first one is the camber arrangement in which the film cooling holes are placed on the camber line. The second arrangement places the film cooling holes close to the suction side. Their final arrangement was a two rows arrangement in which the film cooling holes were placed on the camber line. The upstream and the two rows arrangements showed better performance than the camber arrangement, especially for the higher blowing ratios. Ahn et al. [24] studied film cooling with only tip holes placed on the camber line, only pressure side holes, and both tip & pressure side holes on a squealer tip geometry. Only the holes on the camber line arrangement effectively cooled the cavity floor. Comparing the hole arrangements on the tip and the pressure side showed that the impact of pressure side holes on cooling performance is negligible for the squealer tip design. He [25] investigated the squealer tip with only tip holes and both tip & pressure side holes. He showed that only tip holes could effectively cool the cavity floor.

On the other hand, Park et al. [26] showed that the suction side case had the worst cooling effectiveness. His investigation included the effects of different hole arrangements, such as single row cooling holes along the camber line, near the pressure and suction side rim. They found better film cooling effectiveness when the holes were near the pressure side and inclined to the suction side from the leading edge to the trailing edge. Unlike these studies, Wang et al. [27] investigated the importance of injection position in a honeycomb tip using a turbine cascade. They showed that injection orientation and position changes affect the cooling and tip leakage flow.

Previous studies showed that the locations of film cooling holes significantly affect film cooling effectiveness. Moreover, film cooling can also affect the tip flow structure and change the overall aerodynamic performance of the blade. Considering these situations, a conventional and uncooled squealer blade design with a relatively low aerodynamic loss but high heat transfer on the tip region was selected for an aerothermal optimization study. Details of this specific optimization strategy without tip cooling were reported by Senel et al. in [28]. The current research extends the optimization approach in [28] to a film cooled squealer tip geometry. This study aims to reduce the heat transfer on the tip surface without increasing aerodynamic loss by optimizing the positions of the film cooling holes. For this purpose, five film cooling holes are used, and four of them are optimized in the blade's y-direction, as shown in Figure 8. The fifth one, which is close to the trailing edge, is fixed to reduce the convergence time of the optimization algorithm. Its impact on cooling performance is less than the others, and it has not much space in the y-direction to change cooling performance much with position optimization. This study is a continuation of a previous study [29] which is position optimization of film cooling holes on a squealer turbine blade tip. The thermal boundary conditions were changed for this study, and the impact of casing relative motion and the blowing ratio in heat transfer and aerodynamic loss was also investigated.

## **2. Mathematical Models**

### *2.1. Turbulence Model*

Turbulent flow prediction is crucial for turbomachinery aerodynamics and heat transfer studies. There are many turbulence models for the numerical solution of high Reynolds number turbomachinery flows resolved by Reynolds Averaged Navier Stokes Equations (RANS). The most widely used two-equation models are  $k-\epsilon$  and  $k-\omega$  turbulence models for turbomachinery flows. Wilcox [30] published a comparative study of these models and stated that the  $k-\omega$  model is consistent for all pressure gradients differently from the  $k-\epsilon$  model. Menter [31] also presented an SST  $k-\omega$  model for adverse pressure gradients. The present study used the incompressible SST  $k-\omega$  model of turbulence [31].

### *2.2. Objective Functions & Non-Dimensional Variables*

This section defines the objective functions of the optimization study and the non-dimensional flow and heat transfer parameters. The static pressure coefficient is defined as follows:

$$C_p = \frac{p - p_i}{0.5 \rho U_i^2} \quad (1)$$

where  $p$  is mass-averaged local static pressure.  $p_i$  denotes the mass-averaged static pressure at cascade inlet as the reference pressure of the non-dimensional  $C_p$ . The denominator of equation 1 is the cascade inlet dynamic head, where  $U_i$  is the cascade inlet velocity.

Aerodynamic performance is one of the main objectives of this study. The total pressure coefficient  $C_{p0}$  is described in equation 2, where  $U_m$  is the mean blade speed at midspan, taken from the Axial Flow Turbine Research Facility (AFTRF) of Pennsylvania State University [28]. The total pressure loss coefficient, defined in equation 3, is used to compare the aerodynamic performance of the cases.  $C_{p0}$  is calculated on the plane located at  $0.25 C_x$  downstream from the HP turbine airfoil's trailing edge, as shown in Figure 1. The specific HP turbine airfoil under investigation is identical to the rotor tip profile of the AFTRF test rig [28].

$$C_{p0} = \frac{p_0 - p_{0i}}{0.5 \rho U_m^2} \quad (2)$$

$$\Delta C_{p0} = \frac{\iint \rho u C_{p0} dy dz}{\iint \rho u dy dz} \quad (3)$$

The heat transfer rate on the cavity surface, as defined in equation 7, is another objective of this optimization effort.  $q_w''$  is the rate of thermal energy transfer per unit area per unit time by forced convection. An open-source code is used to calculate wall heat flux in OpenFOAM® [32]. It calculates wall heat flux using turbulent and effective heat conductivity, defined in equations 4 and 5.

$$\kappa_t = \nu_t / Pr_t \quad (4)$$

$$\kappa_{eff} = \nu / Pr + \kappa_t \quad (5)$$

$$q_w'' = \kappa_{eff} C_p \rho \nabla T \quad (6)$$

$$q_w = \iint q_w'' dx dy \quad (7)$$

Solving 3-dimensional complex flow models using CFD takes much time, and many cases should be solved for a multiobjective optimization study. Therefore, an artificial neural network (ANN) is used to efficiently decrease the overall computational time. The neural network uses an initial database that has been generated by using CFD predictions.

### 2.3. Artificial Neural Network & Optimization Algorithm

The created database includes two parts as training and testing. ANN uses training parts to create networks,

and the testing part is used to select the best network. In this study, 70% of the database has been used for testing, and 30% has been allocated for training. The mean square error, defined in equation 8, is used to select the best network.  $\hat{Y}_i$  represents network predictions for testing data, and  $Y_i$  represents the actual testing data obtained using CFD. A Feed Forward Neural Network (FFNN) is used for function approximation. There are many successful optimization studies using FFNN as an approximation tool [33-38]. The neural network package of the open-source software Octave [39] is used for constructing the ANN.

$$MSE = \frac{1}{n} \sum_{i=1}^n (\hat{Y}_i - Y_i) \quad (8)$$

Unlike single-objective versions, multiobjective optimization studies produce more than one optimum solution. The solutions not dominated by other solutions in both objectives are created as Pareto optimal solutions. A non-dominated sorting genetic algorithm NSGA-II [40] is one of the most widely used algorithms for multiobjective optimization studies because of its ability to find convergent solutions to difficult problems [41-43]. It generally uses the Darwinian principle, which selects the fittest and non-dominated solutions, creating Pareto optimal solutions. It also uses crowding distance beside the non-dominated rank to preserve diversity.

### 3. Methodology

#### 3.1. Geometric Details of the HP Turbine Blade

The numerical study's HP turbine blade profile belongs to the Axial Flow Turbine Research Facility (AFTRF) at Pennsylvania State University (Fig. 1). The tip profile of the AFTRF rotor airfoil [44], [45] is used to form an extruded solid model of the blade tip for the present calculations. The design specifications of the linear cascade used throughout the current computations are given in Table 1. A sketch depicting the linear cascade's geometrical parameters is shown in Fig. 1, and the manufacturing coordinates of the tip airfoil section are given in Appendix 1. Senel et al. [28] also used the same tip geometry for another ANN-based aerothermal optimization study.



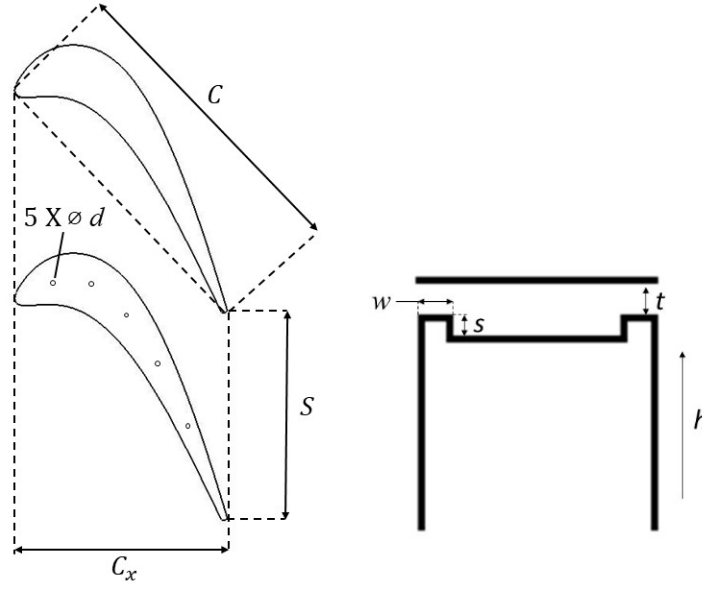


**Figure 1:** Geometric details of the AFTRF tip airfoil.

The numerical study's HP turbine blade profile belongs to the Axial Flow Turbine Research Facility (AFTRF) at Pennsylvania State University (Fig. 1). The tip profile of the AFTRF rotor airfoil [44], [45] is used to form an extruded solid model of the blade tip for the present calculations. The design specifications of the linear cascade used throughout the current computations are given in Table 1. A sketch depicting the linear cascade's geometrical parameters is shown in Fig. 1, and the manufacturing coordinates of the tip airfoil section are given in Appendix 1. Senel et al. [28] also used the same tip geometry for another ANN-based aerothermal optimization study.

**Table 1:** Geometric dimension of turbine blade [28].

<i>Geometric Parameter</i>	<i>Value</i>
Blade Chord, $C$	121.5 mm
Blade Axial Chord, $C_x$	85.04 mm
Blade Span, $h$	123 mm
Blade Pitch, $S$	99.274 mm
Tip Clearance, $t$	1.23 mm
Squealer Width, $w$	2.101 mm
Squealer Height, $s$	1.2 mm
Inlet Flow Angle, $\alpha$	71.3°
Film Cooling Hole Diameter, $d$	1.125 mm

The computational domain in this investigation is formed as a linear turbine cascade arrangement. Special attention is paid to generating film cooling holes in the squealer tip cavity. A periodic boundary condition is imposed in the circumferential direction in the linear cascade configuration. A typical linear cascade arrangement

corresponds to a flow system with an infinite number of blades where perfect circumferential periodicity exists. The relative inlet flow conditions to the AFTRF rotor are simulated in the cascade.

The rotor inlet conditions are shown in Table 2. While the ratio between film cooling inlet temperature and inlet temperature is 0.5, wall temperature and inlet temperature are 0.7. The computational domain in this investigation is formed as a linear turbine cascade arrangement.

Holes are positioned with 14 mm spacings throughout axial chord length as from the leading edge, and positions of 4 film cooling holes on the y-direction of the blade are free to use as optimization variables. 5<sup>th</sup> hole, which is close to the trailing edge, is fixed on a specific position.

**Table 2:** Initial conditions.

<i>Geometric Parameter</i>	<i>Value</i>
Inlet Velocity	(27.2, 8.6, -2.2) m/s
Outlet Pressure	-3595 Pa
Inlet Temperature	440 °K
Wall Temperature	308 °K
Film Cooling Inlet Temperature	220 °K
Blowing Ratio ( $M=\rho_c U_c / \rho_\infty U_\infty$ )	1

### 3.2. Grid Generation

For an optimization study, many analyses are required to optimize the objectives, and the number of analyses increases with an increasing number of input variables. Four input variables exist in the present study. These are normalized film cooling hole positions between the suction side and pressure. The subsequent computational runs usually increase the computational cost and elapsed time of the optimization process. Grid generation is typically required each time when positions of film cooling holes are changed. However, *topoSet* and *createPatch* utilities of the OpenFOAM® software provide a solution to change the cooling positions without requiring new grid generation at each step. This automatic grid updating feature significantly lightens the computational effort. A new grid is generated with densification on the lines where the positions of film cooling holes are optimized. The fifth line close to the trailing edge is not used for the optimization. The location of the cooling hole on the fifth line is fixed on the mean camber line. The grid structure and a detailed view of the cooling hole region are given in Figure 2.

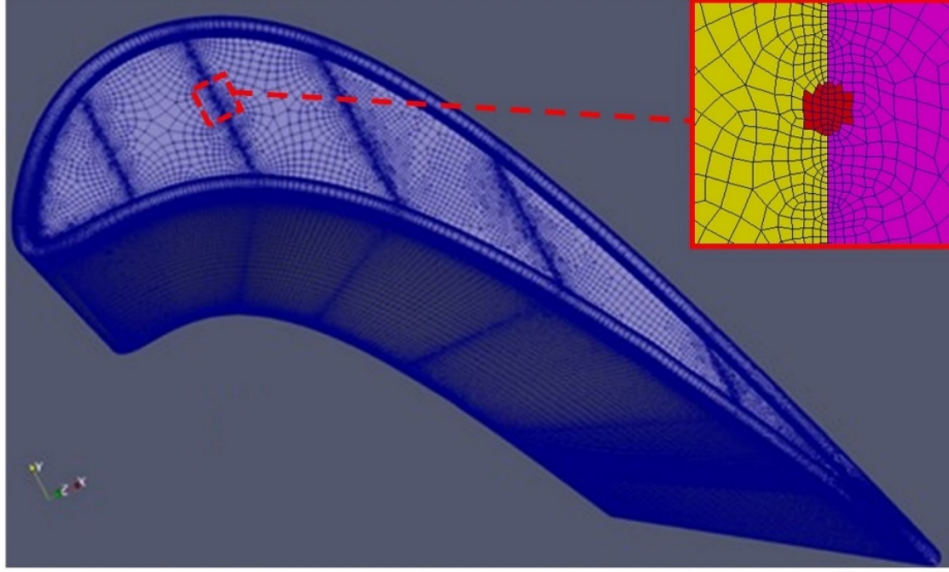


**Figure 2:** Generated grid of current study and the cooling hole region.

A mesh dependency test was carried out with 6.7, 7.2, 7.8 and 8.4 million cells. The static pressure coefficient distributions at mid-span from each grid measure are shown in Figure 3. There is almost no difference between the results with different mesh densities. Therefore, the mesh with 7.8 million cells was selected to run the cases because of the densification necessity of *topoSet* utility. The average  $y^+$  value on the tip section is around 0.13 for the generated grid.

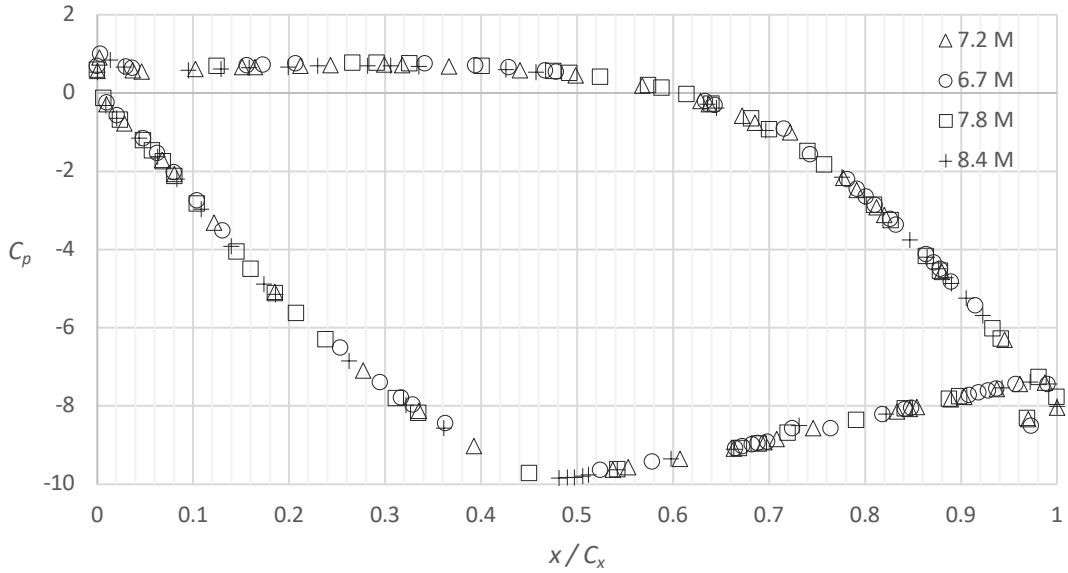


**Figure 3:** Mesh independence,  $C_p$  versus  $x/C_x$  around the mid-span.

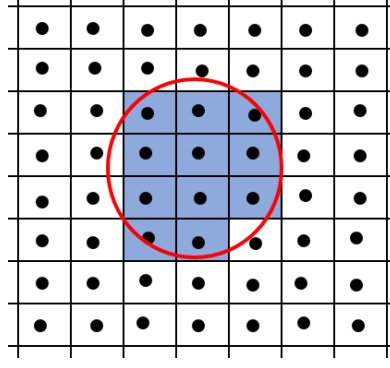


**Figure 4:** Representation of cylindrical selection.

### 3.3. Automated grid updates for new cooling hole locations

The same grid has been used for all cases with automated modifications required for different film cooling hole locations. Automatic grid modifications effectively reduce total optimization time and complexity. The *topoSet* utility of OpenFOAM® is used with a cylindrical selection option, and cell faces are selected on the lines where the grid densification was imposed. Representation of cylindrical selection of *topoSet* utility can be shown in Figure 4. After that, the selected faces boundary type is changed from wall to inlet by using *createPatch* utility of OpenFOAM® repeated for all film cooling inlets.

However, this technique has many disadvantages because the mesh structure does not become a perfect circle around the cooling hole, as shown in Figure 4, after subsequent updates. Thus, the mesh structure is kept denser on the lines on which the positions of film cooling holes are optimized. The RANS computation time per case increases because of artificially increased mesh density. However, an automated update is still better than generating a brand-new mesh for all cases. The effect of the slight geometric difference of holes in the updated mesh structure is neglected in this study. The relative standard deviations of mass flow rates are separately 4.7%, 4.3%, 3.1% and 5.4% from the 1<sup>st</sup> to 4<sup>th</sup> film cooling hole.

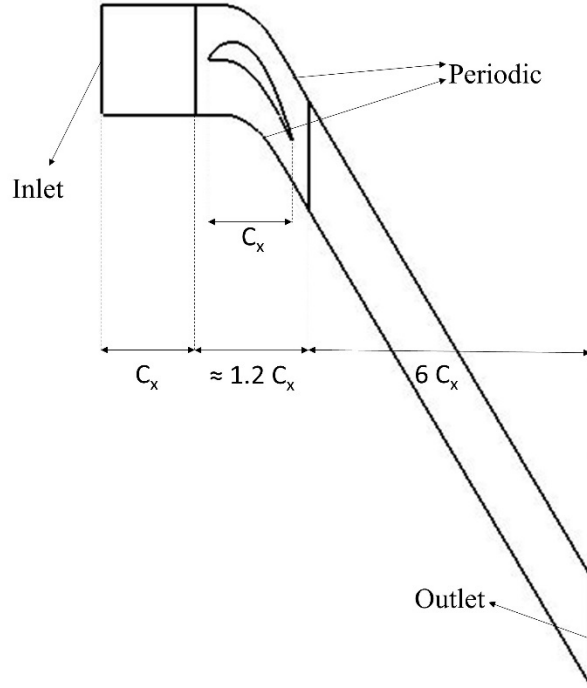


**Figure 5:** Boundary conditions on the computational domain forming the linear cascade of the AFTRF tip profile.

### 3.4. Boundary & Initial Conditions

Figure 5 shows the computational domain of the cascade model with boundary conditions. The domain is divided into three parts as inlet, rotor, and outlet. The domain's sides are imposed as periodic boundary conditions by the cascade flow assumptions, and other boundaries are defined as no-slip walls except inlet and outlet.

Velocity inlet and pressure outlet conditions are used at the inlet and exit of the domain. Initial values of boundary conditions are given in Table 2, and the turbulence intensity of the inlet is set to 0.5% as measured in the AFTRF operation [44], [45], [28].

The blowing ratio is a critical variable that changes cooling performance because the coolant flow should have enough energy to surpass tip flow and create a proper coolant layer on the tip surface. Many studies showed that increasing the blowing ratio increases the cooling performance [18], [19], [20]. However, over an optimal injection rate, the film coolant penetrates the free stream, and it starts to lose its cooling effectiveness near the wall. A high blowing ratio also reduces the turbine efficiency by consuming too much pressurized air from the cycle. The blowing rate was selected as one throughout this optimization approach.

On the other hand, the low blowing ratio case, which is 0.4, and casing relative motion were also studied to see their effects on aerodynamic performance and heat transfer on the tip region after the optimization process. The speed of the casing relative motion is taken from AFTRF parameters [46] which is 63.5 m/s, calculated from a rotational speed of

1322 rpm.

### 3.5. Validation of the Aero-heat Transfer Effort

**Aerodynamic Validation:** Validation of the CFD effort was performed using a turbine blade profile that has been experimentally studied by Beer [47]. The predicted uncertainty  $\delta C_p$  is 0.6% for pressure measurements. The  $C_p$  distribution measured at the mid-span of the airfoil in a linear cascade arrangement was compared to the current computational aerodynamics data. Figure 6 compares the experimental results and the current three-dimensional CFD simulation of the static pressure coefficient at the mid-span. The computed  $C_p$  over the airfoil surfaces follows the experimental measurement points well. There is a slight discrepancy over  $x/C_x=0.7$  on the aft part of the airfoil suction side. This region corresponds to a diffusion zone with a mild adverse pressure gradient. However, this slight discrepancy is within the measurement error.

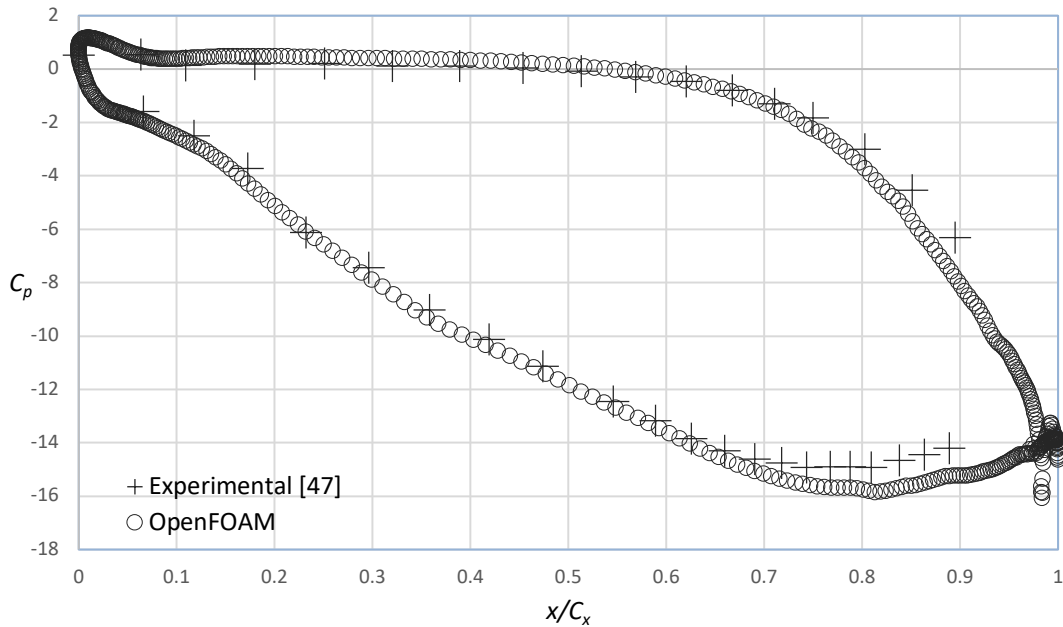


**Figure 6:** Comparison between experimental blade loading data [47]  $C_p$  and current OpenFOAM® results.

**Heat Transfer Validation:** On the other hand, validation of heat transfer is also important for this study. An experimental heat transfer data set on the suction side of the SM701 airfoil obtained by Klaput [48], which has a 304.8 mm chord length, is used to validate the current heat transfer computations. This airfoil was selected because of the availability of high-resolution convective heat transfer data on its suction side. The experimental heat transfer data set was obtained in a wind tunnel experiment by [48]. This experiment simultaneously included laminar, transitional and turbulent flow zones on its suction side. The predicted uncertainty  $\delta h$  is 6% for heat transfer measurements. The airfoil coordinates of SM701, originally designed by Maughmer and Somers

[49],[50] are listed in Appendix-2. The heat transfer coefficient on the suction side of the SM701 airfoil is compared to the CFD result in Figure 7. The suction side of the specific airfoil simultaneously contains the laminar, transitional and fully turbulent zones making the prediction of convective heat transfer rates a challenging experimental task. Langtry-Menter shear stress transport model [51] was used in this validation study. There is a slight difference in the start of the laminar region from the leading edge to the  $x/C_x=0.2$ . After this region, CFD and experimental results show pretty similar profiles, and CFD results also catch the transition and turbulence region till  $x/C_x=0.8$ . Between  $x/C_x=0.8$  and 1, the fully turbulent region starts with the addition of some trailing edge separation. Although this makes it harder to properly solve and converge the flow with the CFD model in this region, the CFD model properly catches the general trends of  $h$ . The region after  $x/C_x=0.80$  is a relatively high uncertainty zone for the heat transfer experiments because the copper electrodes of the Inconel constant heat flux surface tend to slightly disturb the otherwise smooth heat transfer surface.

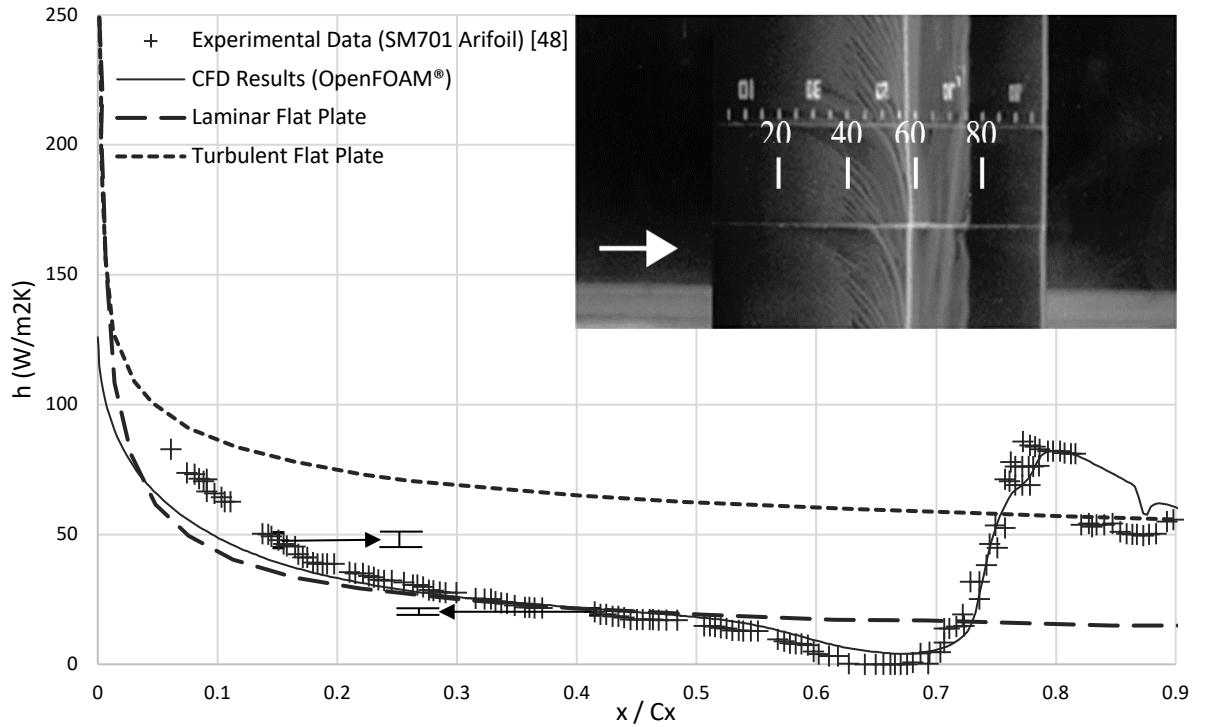


**Figure 7:** Comparison between experimental heat transfer data [48] and present OpenFOAM® results of the suction surface of SM701 airfoil.

### 3.6. Optimization Process

An initial database consisting of 21 cases is created for the optimization process, and Latin hypercube sampling [52] is used to specify the values of inputs for these cases. After the first optimization process, three design points are selected from the Pareto curve and checked for their CFD results. These new three design points and their

CFD solutions are added to the database, and optimization is repeated. This loop continues till the difference between CFD and ANN results decreases below 1%. The positions of the four film cooling holes on the y-direction are normalized between 0 and 1, as shown in Figure 8. Table 3 shows the normalized values used as input parameters. The fifth hole is not used as a design variable, and its position is fixed to decrease the number of computational runs and the optimization cost. The fifth hole is in a narrow region near the trailing edge wedge zone. The manufacturing limitations may not allow flexibility to change its position easily. The ANN created contains four input neurons, two output neurons, and a hidden layer consisting of hidden neurons between 1 and 10. The networks were trained ten times for each hidden layer configuration, and the ANN with the minimum overall error was selected. NSGA-II algorithm is used for the optimization process with the best network. The population contains 100 individuals, and the process is run for 200 generations.

**Table 3:** Design points of film cooling holes.

<i>Design Points</i>					<i>Design Points</i>				
<i>Case #</i>	<i>(Normalized Between 0 and 1)</i>				<i>Case #</i>	<i>(Normalized Between 0 and 1)</i>			
	<i>1<sup>st</sup> Hole</i>	<i>2<sup>nd</sup> Hole</i>	<i>3<sup>rd</sup> Hole</i>	<i>4<sup>th</sup> Hole</i>		<i>1<sup>st</sup> Hole</i>	<i>2<sup>nd</sup> Hole</i>	<i>3<sup>rd</sup> Hole</i>	<i>4<sup>th</sup> Hole</i>
1	0.4992	0.6890	0.0344	0.7471	27	0.0488	0.5713	0.1790	0.2920
2	0.7146	0.9571	0.0432	0.2347	28	0.0840	0.0000	0.4411	0.4217
3	0.8641	0.0219	0.7375	0.9913	29	1.0000	1.0000	0.0000	0.0000
4	0.6685	0.6461	0.4258	0.8051	30	0.3456	0.2985	0.0000	0.9076
5	0.3486	0.3075	0.3515	0.3113	31	0.0008	1.0000	0.7105	0.9975
6	0.4094	0.8708	0.6969	0.6186	32	0.0979	0.9113	0.0000	0.9357
7	0.6221	0.2373	0.2986	0.4326	33	0.4349	0.1567	0.1651	1.0000
8	0.1200	0.4381	0.4702	0.8265	34	1.0000	1.0000	1.0000	1.0000
9	0.0842	0.4218	0.6093	0.2856	35	0.4633	0.0463	0.0838	0.4102
10	0.2192	0.8344	0.7624	0.0938	36	0.3921	0.7527	0.2568	0.5747
11	0.4426	0.7973	0.2558	0.5615	37	0.3505	0.0000	0.2592	0.7526
12	0.9734	0.2681	0.5689	0.8831	38	0.6481	0.0000	0.6182	0.2880
13	0.5830	0.3494	0.8245	0.1844	39	0.3401	0.0000	0.7686	0.0000
14	0.2859	0.0872	0.1007	0.3805	40	0.2081	0.6324	0.4485	0.4500
15	0.2399	0.7486	0.5072	0.6320	41	0.1948	0.5323	0.3962	0.4285
16	0.8317	0.6096	0.3898	0.0308	42	0.5039	0.0000	0.2058	0.6021
17	0.9065	0.1812	0.2357	0.9152	43	0.4972	0.3085	0.2917	0.5805
18	0.5659	0.1273	0.1788	0.6935	44	0.5289	0.1947	0.2816	0.6182
19	0.1880	0.4819	0.6308	0.5030	45	0.5242	0.2361	0.3889	0.6313
20	0.0331	0.9299	0.8577	0.1405	46	0.5498	0.3490	0.3819	0.6527
21	0.7819	0.5522	0.1451	0.4262	47	0.5447	0.3482	0.3800	0.7153
22	0.8491	0.0788	0.0000	0.0000	48	0.6013	0.3968	0.0190	0.8543
23	0.2069	1.0000	1.0000	0.0000	49	0.5633	0.3661	0.0173	0.8638
24	0.0000	0.9995	0.8732	0.0009	50	0.5145	0.4236	0.0163	0.8621
25	0.0000	1.0000	1.0000	0.7576	<i>5th Hole is fixed on 0.3475</i>				
26	0.0601	0.0000	0.0000	0.0000					



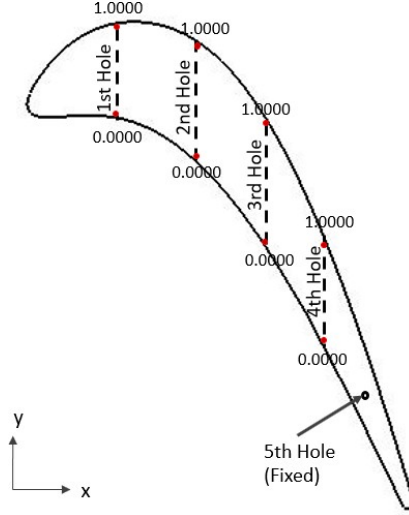


**Figure 8:** Normalization of hole positions between 0 and 1.

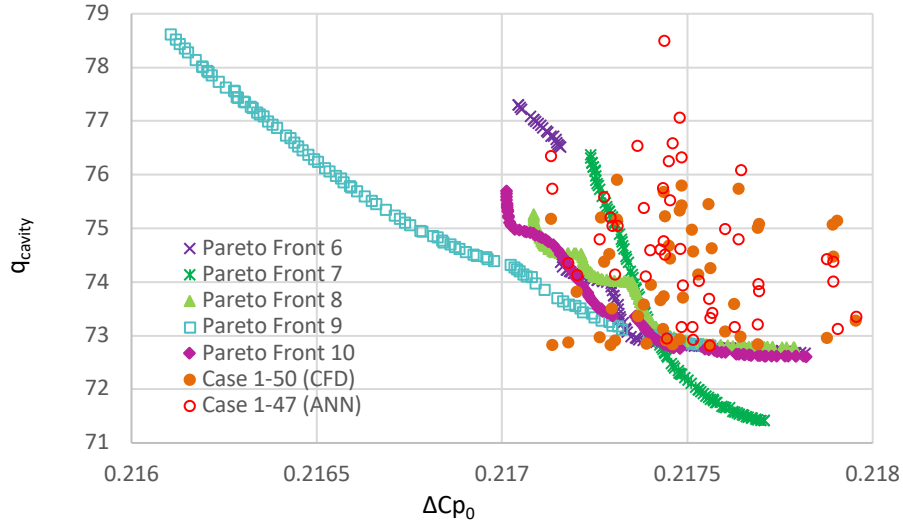


**Figure 9:** Pareto optimal solutions and results.

The current optimizations' objective functions are the total pressure loss coefficient and the integrated wall heat flux on the cavity surface. Figure 9 presents the last five of the Pareto fronts created using NSGA-II and all CFD results. The input values of the best heat transfer rate solution of the final Pareto front are taken and tested with CFD in the 50<sup>th</sup> case. The relative error between optimization predictions and CFD results is decreased to less than 1%.

On the other hand, the relative difference between the aerodynamic loss coefficients of the cases is more diminutive. Thus, the neural network algorithm sees the differences as errors and cannot produce a neural network at the exact points of aerodynamic loss coefficients. The red points in Figure 9 show how the neural network predicts 47 cases before the last iteration.

#### 4. Results and Discussion

**Table 4:** Results of optimization objectives ( $\Omega$  and  $\Gamma$  values show the relative difference with respect to Case 0).

<i>Case # (i)</i>	$\Delta C_{p0}$	$\Omega$	$q_{cavity}$	$q_{tip}$	$q_{side}$	$q_{total}$	$\Gamma$
0 (NO FC)	-0.21663	<b>0.00%</b>	-38.78	-31.93	-13.40	-84.11	<b>0.00%</b>
1	-0.21731	<b>0.31%</b>	-33.77	-29.59	-11.69	-75.05	<b>-10.77%</b>
2	-0.21713	<b>0.23%</b>	-34.76	-29.53	-11.44	-75.74	<b>-9.95%</b>
3	-0.21764	<b>0.47%</b>	-35.28	-29.51	-11.30	-76.09	<b>-9.53%</b>
4	-0.21726	<b>0.29%</b>	-33.45	-29.62	-11.73	-74.80	<b>-11.07%</b>
5	-0.21763	<b>0.46%</b>	-31.44	-29.86	-11.86	-73.16	<b>-13.02%</b>
6	-0.21738	<b>0.35%</b>	-33.93	-29.60	-11.84	-75.38	<b>-10.38%</b>
7	-0.21756	<b>0.43%</b>	-31.90	-29.75	-11.66	-73.31	<b>-12.83%</b>
8	-0.21753	<b>0.41%</b>	-32.55	-29.78	-11.70	-74.02	<b>-11.99%</b>
9	-0.21730	<b>0.31%</b>	-32.69	-29.78	-11.67	-74.14	<b>-11.85%</b>
10	-0.21727	<b>0.30%</b>	-34.56	-29.52	-11.52	-75.60	<b>-10.12%</b>
11	-0.21744	<b>0.37%</b>	-33.20	-29.70	-11.85	-74.75	<b>-11.12%</b>
12	-0.21743	<b>0.37%</b>	-34.25	-29.74	-11.76	-75.76	<b>-9.93%</b>
13	-0.21720	<b>0.26%</b>	-32.82	-29.64	-11.66	-74.12	<b>-11.87%</b>
14	-0.21769	<b>0.49%</b>	-31.97	-29.73	-11.51	-73.21	<b>-12.95%</b>
15	-0.21718	<b>0.25%</b>	-33.02	-29.63	-11.69	-74.34	<b>-11.61%</b>
16	-0.21745	<b>0.38%</b>	-34.45	-29.50	-11.58	-75.52	<b>-10.21%</b>
17	-0.21760	<b>0.45%</b>	-33.98	-29.56	-11.45	-74.99	<b>-10.84%</b>
18	-0.21752	<b>0.41%</b>	-31.84	-29.61	-11.46	-72.91	<b>-13.31%</b>
19	-0.21743	<b>0.37%</b>	-33.04	-29.79	-11.77	-74.59	<b>-11.31%</b>
20	-0.21713	<b>0.23%</b>	-35.44	-29.49	-11.42	-76.35	<b>-9.22%</b>
21	-0.21729	<b>0.30%</b>	-33.84	-29.64	-11.56	-75.04	<b>-10.78%</b>
22	-0.21764	<b>0.46%</b>	-34.53	-29.20	-11.06	-74.79	<b>-11.07%</b>
23	-0.21748	<b>0.39%</b>	-35.62	-29.46	-11.25	-76.33	<b>-9.25%</b>
24	-0.21745	<b>0.38%</b>	-35.57	-29.36	-11.32	-76.25	<b>-9.34%</b>
25	-0.21737	<b>0.34%</b>	-35.51	-29.64	-11.38	-76.53	<b>-9.01%</b>
26	-0.21789	<b>0.58%</b>	-34.25	-29.20	-10.92	-74.38	<b>-11.57%</b>
27	-0.21748	<b>0.39%</b>	-33.45	-29.66	-11.51	-74.61	<b>-11.29%</b>
28	-0.21788	<b>0.57%</b>	-33.25	-29.72	-11.45	-74.42	<b>-11.52%</b>
29	-0.21748	<b>0.39%</b>	-36.36	-29.35	-11.34	-77.06	<b>-8.38%</b>
30	-0.21748	<b>0.39%</b>	-32.37	-29.42	-11.37	-73.15	<b>-13.02%</b>
31	-0.21746	<b>0.38%</b>	-35.53	-29.66	-11.40	-76.59	<b>-8.94%</b>
32	-0.21729	<b>0.31%</b>	-34.98	-29.21	-11.01	-75.20	<b>-10.59%</b>
33	-0.21749	<b>0.40%</b>	-32.87	-29.66	-11.40	-73.93	<b>-12.10%</b>
34	-0.21744	<b>0.37%</b>	-37.29	-29.73	-11.46	-78.48	<b>-6.68%</b>
35	-0.21769	<b>0.49%</b>	-32.70	-29.64	-11.49	-73.83	<b>-12.22%</b>
36	-0.21744	<b>0.37%</b>	-33.06	-29.64	-11.81	-74.50	<b>-11.42%</b>
37	-0.21795	<b>0.61%</b>	-32.14	-29.69	-11.52	-73.35	<b>-12.79%</b>
38	-0.21769	<b>0.49%</b>	-33.07	-29.54	-11.36	-73.96	<b>-12.06%</b>
39	-0.21789	<b>0.58%</b>	-33.23	-29.42	-11.36	-74.01	<b>-12.01%</b>
40	-0.21740	<b>0.36%</b>	-33.09	-29.76	-11.74	-74.58	<b>-11.32%</b>
41	-0.21739	<b>0.35%</b>	-32.60	-29.78	-11.72	-74.10	<b>-11.90%</b>
42	-0.21756	<b>0.43%</b>	-32.51	-29.68	-11.49	-73.69	<b>-12.39%</b>
43	-0.21790	<b>0.59%</b>	-31.54	-29.79	-11.79	-73.12	<b>-13.06%</b>
44	-0.21756	<b>0.43%</b>	-31.45	-29.71	-11.65	-72.81	<b>-13.43%</b>
45	-0.21751	<b>0.41%</b>	-31.55	-29.80	-11.80	-73.15	<b>-13.02%</b>
46	-0.21757	<b>0.43%</b>	-31.70	-29.87	-11.86	-73.43	<b>-12.70%</b>
47	-0.21744	<b>0.38%</b>	-31.42	-29.74	-11.77	-72.94	<b>-13.28%</b>
48	-0.21727	<b>0.29%</b>	-32.12	-29.49	-11.33	-72.95	<b>-13.27%</b>
49	-0.21731	<b>0.31%</b>	-32.42	-29.53	-11.37	-73.32	<b>-12.83%</b>
50	-0.21730	<b>0.31%</b>	-32.21	-29.56	-11.45	-73.22	<b>-12.95%</b>

CFD results of the cases with different positions of film cooling holes and the case without film cooling holes are listed in Table 4.  $\Omega$  and  $\Gamma$  show the difference in total pressure loss coefficient and heat transfer rate of tip surface between the Case 0 and the related case.  $q_{cavity}$ ,  $q_{tip}$  and  $q_{side}$  show respectively the heat transfer rate on the cavity surface of the squealer tip, heat transfer rate on the tip surface, which is the closest surface of the squealer tip to the casing and heat transfer rate on the side surface, which is step surface between tip and cavity surface of squealer tip. The case without film cooling holes is represented as Case 0. Improvements in both heat transfer rate at the tip and total pressure loss coefficient with film cooling addition are apparent. On the other hand, there is no significant change between the total heat transfer coefficients of the cases with film cooling holes because the flow through the holes is defined as normal to the cavity surface. Also, the coolant effect on leakage flow does not change much in different positions. The maximum difference rate between the total pressure loss coefficients of the cases with film cooling is 0.61%. Therefore, the best case selected by looking at the cooling performance was Case 44 in Table 4.

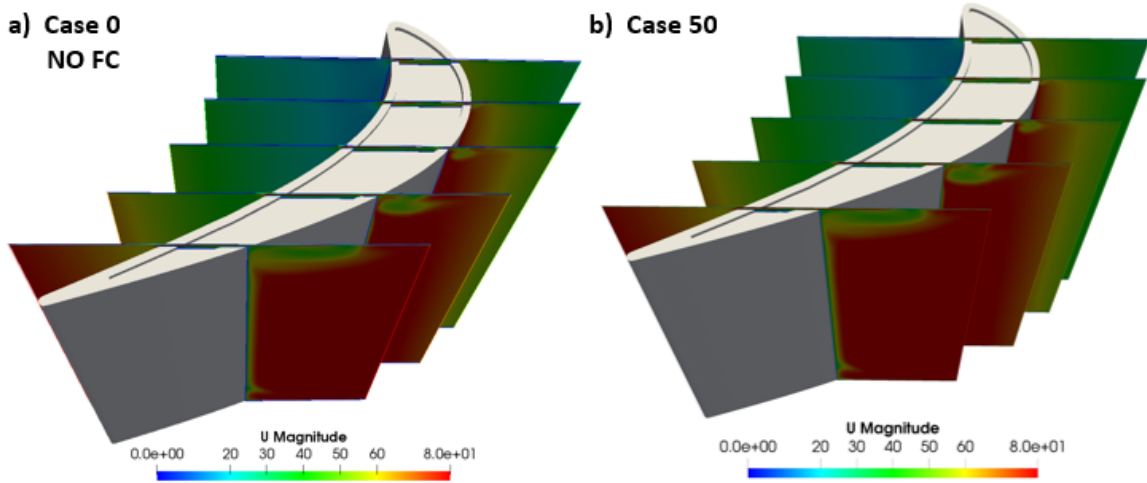


**Figure 10:** Velocity contours at planes where film cooling holes are located, a) No film cooling case b) Case 50.

The velocity contour on five sections where film cooling holes are located is shown in Figure 10. There is a slight difference in the velocity contour where the leakage vortex occurs. This difference especially shows itself in the fifth section, close to the trailing edge.

On the other hand, the total pressure loss coefficient is an essential variable for the aerodynamic behavior of the blade, and it is shown at the exit plane in Figure 11. The blue region in Figure 11 is the area affected by the tip leakage flow. Compared to Case0, the blue region slightly enlarges with the addition of coolant to the leakage flow. In addition to this, the difference between the suction and pressure side is straighter and sharper in Case 0, and it shows that the effect of secondary flows is more negligible in Case 0. The decrease in the total pressure

coefficient in Case 50 is apparent.

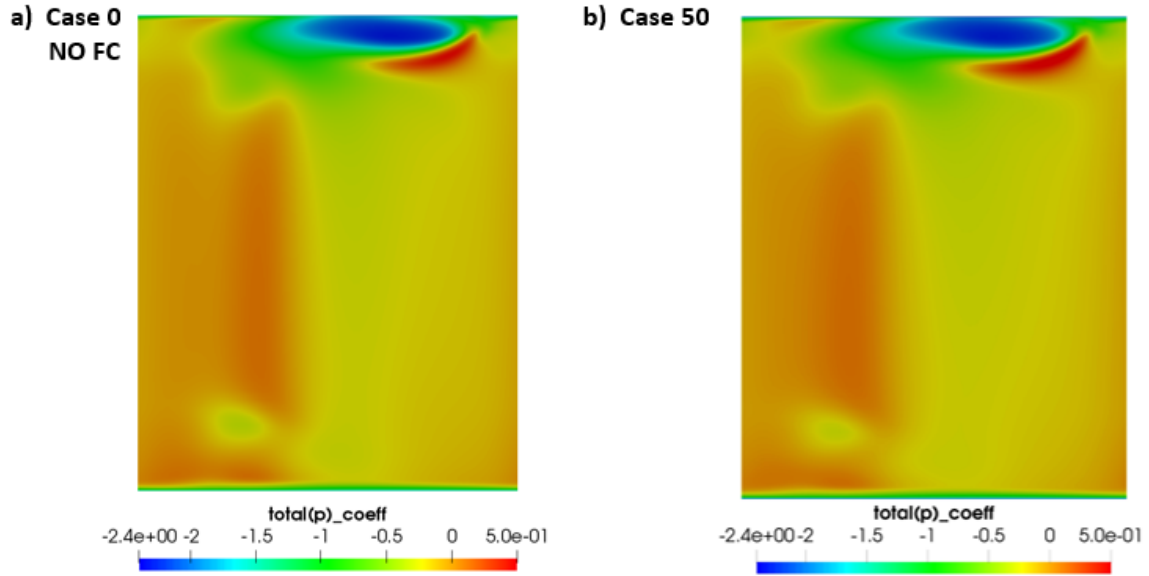


**Figure 11:** Total pressure coefficients at exit plane  $0.25C_x$  downstream, a) No film cooling case b) Case 50.

The effect of leakage flow on the total pressure coefficient at the exit plane is clearly shown in Figure 12. The pressure side horseshoe vortex pushes leakage flow to the pressure side, but it is less effective in Case 0. Because of that, the effects of the leakage vortex on the pressure side of the exit plane increase and show a smooth transition between the right side and left side of the exit plane. More significant adverse pressure gradients occur in this area, and the flow near the pressure side becomes more turbulent.

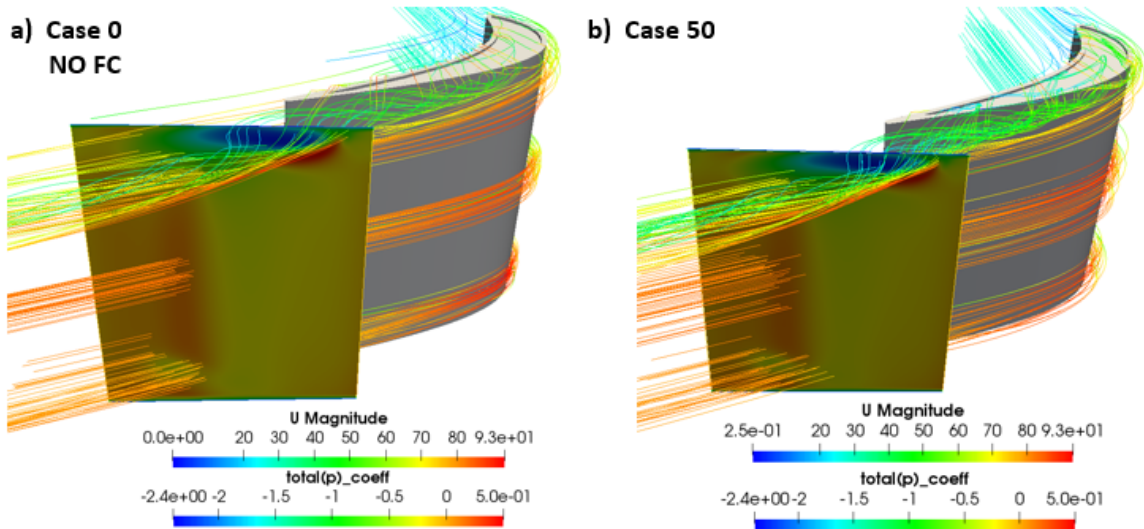


**Figure 12:** Total pressure coefficients at exit plane ( $0.25C_x$  downstream) with streamlines, a) No film cooling case b) Case 50.

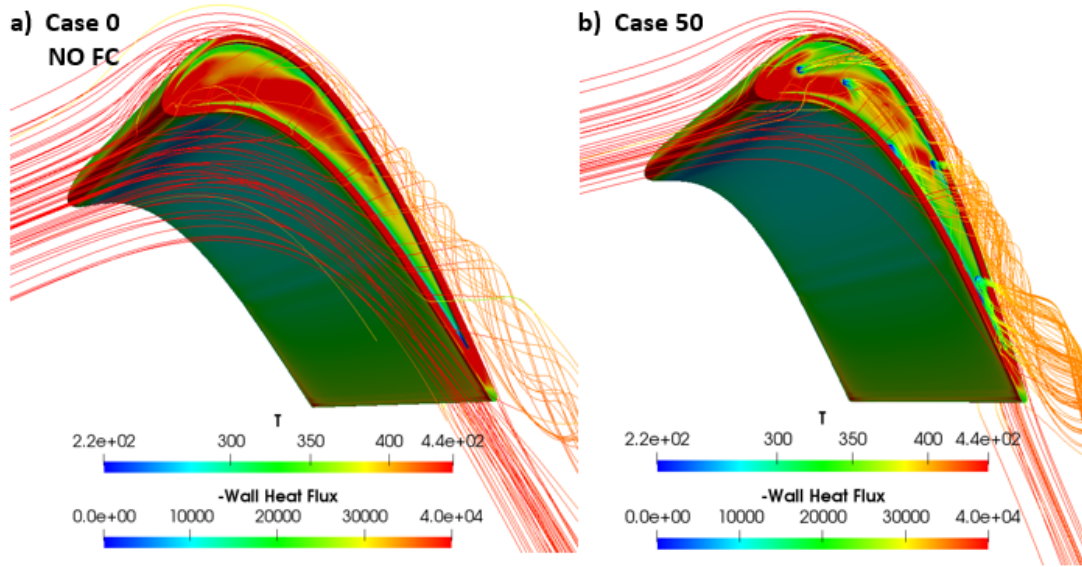


**Figure 13:** Wall heat flux on the blade and streamlines color-coded with temperature. a) No film cooling case b) Case 50.

On the other hand, the main objective of film cooling is to protect surfaces from hot fluid, and wall heat flux is used in this study to understand which zones can be protected by using film cooling. Figure 13 shows the absolute value of wall heat flux on blades. The streamlines are color-coded with temperature. Film cooling effectively decreases wall heat flux at the tip surface, and the heat transfer rate at the tip surface decreases with this reduction. As mentioned in previous sections, film cooling can protect not only where it is injected but also downstream of the injection location, and this can be clearly shown in Figure 13. Wall heat flux decreases where film cooling flow goes, and the heat transfer rate on the leading edge of the tip surface is still high because of the same reason.

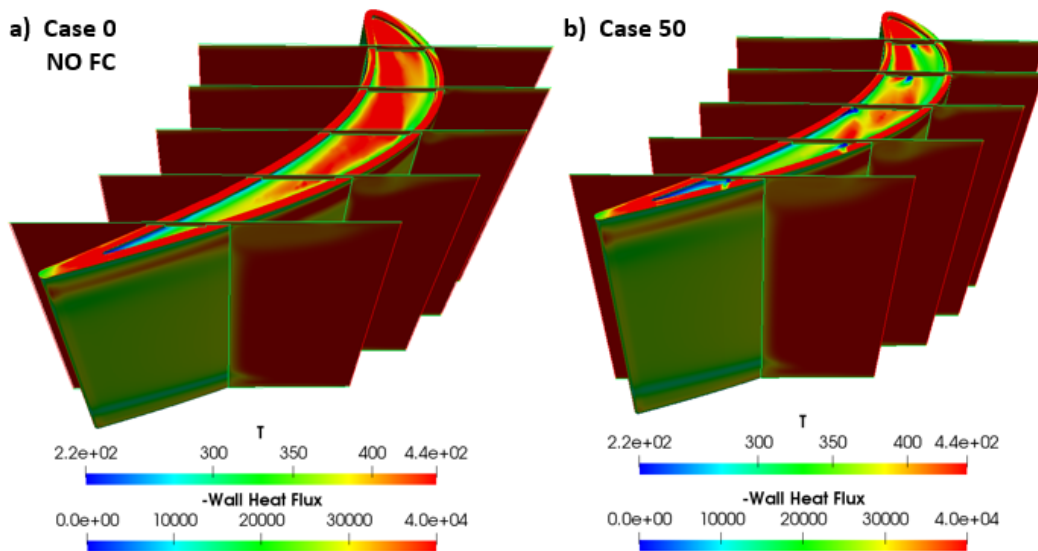


**Figure 14:** Wall heat flux on blade and temperature contours at planes where film cooling holes are located, a) No film cooling case b) Case 50.

In addition to this, it is not a good approach to place film cooling holes close to the pressure or suction side of the cavity surface regarding these results. Because the impact of film cooling holes is less due to the pressure side is in the separation zone of leakage flow, and the suction side is the end of leakage flow. Especially near the trailing edge, the cavity surface narrows and tip leakage flow cannot contact the cavity surface. However, the squealer tip cannot achieve decreasing tip leakage flow in this region because of that.

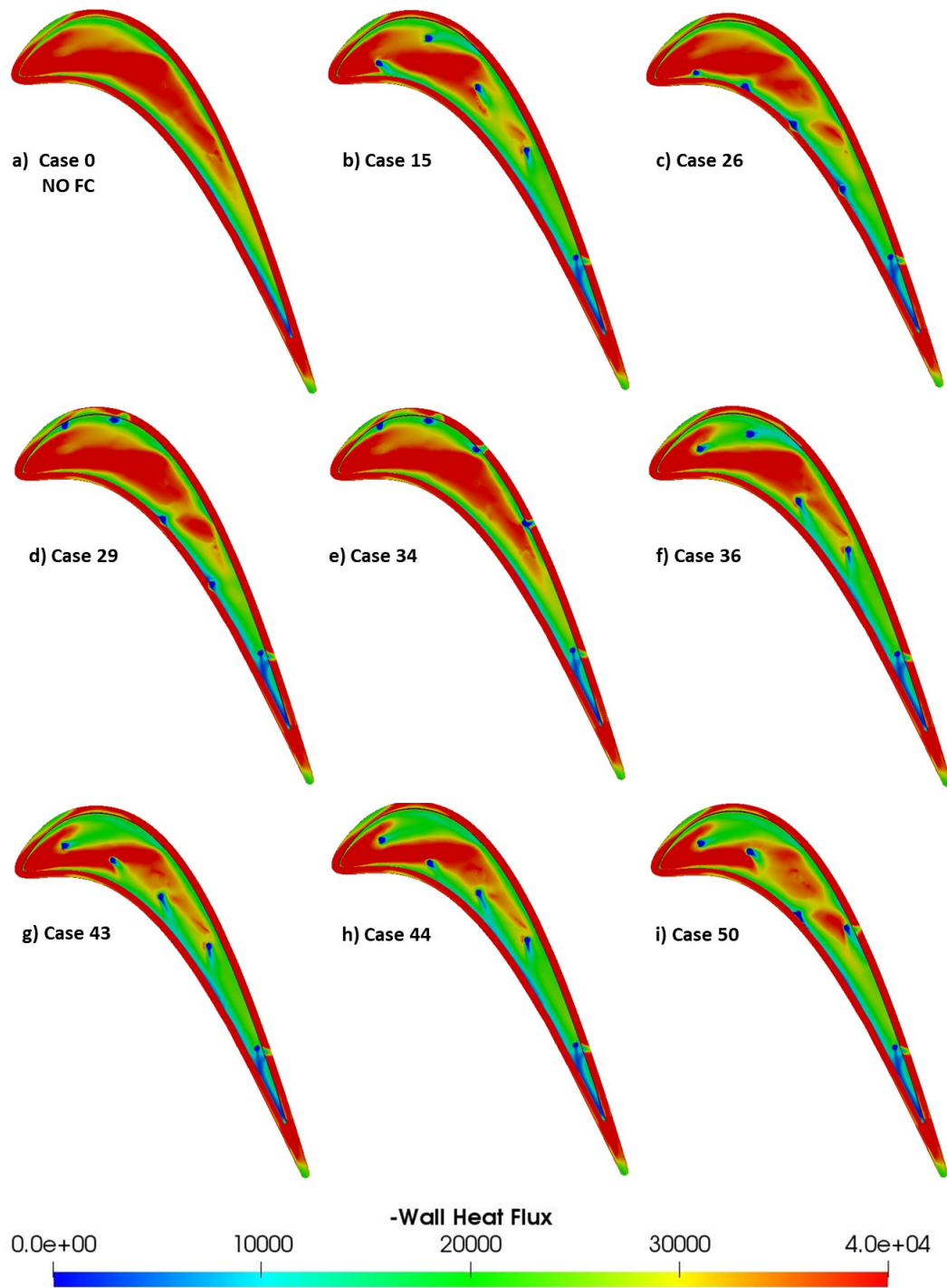


**Figure 15:** Absolute heat transfer rate on tip surface of different cases.

Figure 14 shows the wall heat flux and temperature contours at the section planes where film cooling holes are located. There is a slight difference between Case 0 and Case 50, the same as Figure 10. However, the addition of coolant mass to the tip leakage vortex is more evident when compared to that in Figure 10. With the addition of coolant mass, the vortex takes a more circular shape and gets closer to the suction side.

This study applies position optimization to protect the tip surface without decreasing aerodynamic performance. Wall heat fluxes at the tip surface for some cases from the optimization study are shown in Figure 15, and the results show the effect of film cooling hole positions on cooling performance.

Case 34 has the highest heat transfer rate at the cavity surface between the cases with film cooling. The first four film cooling holes are created quite close to the suction side. This positioning makes them less effective in protecting the surface because they directly join the leakage vortex from the suction side without creating a film layer on the cavity surface. In addition, the coolant flow through the fifth hole, which is fixed, is divided into two parts. One of them goes through the edge of the pressure side, and the other one joins the leakage flow from the suction side. The part that goes to the pressure side decreases wall heat flux on its route. On the other hand, Case 26 has the first four film cooling holes near the pressure side, and it is also not the best cooling case in this study because they are placed in the separation zone, and a significant part of the coolant mass flow goes through the trailing edge near the pressure side rim by joining the separation vortex. As shown in Figure 15, the hole that is so close to the pressure or suction side of the cavity does not effectively protect the cavity surface because the coolant flow of holes near the pressure side sticks to the inner wall of the rim and the coolant flow of holes that near the suction side goes directly out from cavity with the effect of leakage flow.

The position of the first film cooling hole is more important than others because it affects more regions in downstream locations, allowing it to access larger areas on the cavity surface. There is a critical position where the leakage flow changes direction from the suction side to the pressure side for the first hole. In that critical position, it cools a larger area, as shown in 43, 44 and 50. If it comes closer to the pressure side, its protection area is suddenly reduced, as shown in Case 15.

**Table 5:** The results with BR=1 and without casing relative motion ( $\Omega$  and  $\Gamma$  values show the relative difference when compared to the cases that run without casing relative motion and BR=1).

<b>Case # (i)</b>	<b><math>\Delta C_{p0}</math></b>	<b><math>\Omega</math></b>	<b><math>q_{cavity}</math></b>	<b><math>q_{tip}</math></b>	<b><math>q_{side}</math></b>	<b><math>q_{total}</math></b>	<b><math>\Gamma</math></b>
18	-0.21752	<b>0.00%</b>	-31.84	-29.61	-11.46	-72.91	<b>0.00%</b>
44	-0.21756	<b>0.00%</b>	-31.45	-29.71	-11.65	-72.81	<b>0.00%</b>
47	-0.21744	<b>0.00%</b>	-31.42	-29.74	-11.77	-72.94	<b>0.00%</b>

**Table 6:** The results with BR=0.4 and without casing relative motion ( $\Omega$  and  $\Gamma$  values show the relative difference when compared to the cases that run without casing relative motion and BR=1).

<i>Case # (i)</i>	$\Delta C_{p0}$	$\Omega$	$q_{cavity}$	$q_{tip}$	$q_{side}$	$q_{total}$	$\Gamma$
18	-0.21783	<b>0.14%</b>	-34.24	-30.50	-12.25	-76.98	<b>5.58%</b>
44	-0.21745	<b>-0.05%</b>	-34.35	-31.04	-12.61	-78.00	<b>7.13%</b>
47	-0.21740	<b>-0.02%</b>	-34.21	-31.06	-12.68	-77.96	<b>6.88%</b>

**Table 7:** The results with BR=1 and with casing relative motion ( $\Omega$  and  $\Gamma$  values show the relative difference when compared to the cases that run without casing relative motion and BR=1).

<i>Case # (i)</i>	$\Delta C_{p0}$	$\Omega$	$q_{cavity}$	$q_{tip}$	$q_{side}$	$q_{total}$	$\Gamma$
18	-0.23576	<b>8.39%</b>	-25.39	-28.80	-10.08	-64.28	<b>-11.85%</b>
44	-0.23565	<b>8.31%</b>	-26.51	-28.93	-10.50	-65.94	<b>-9.44%</b>
47	-0.23563	<b>8.36%</b>	-26.67	-28.88	-10.50	-66.05	<b>-9.44%</b>

**Table 8:** The results with BR=0.4 and with casing relative motion ( $\Omega$  and  $\Gamma$  values show the relative difference when compared to the cases that run without casing relative motion and BR=1).

<i>Case # (i)</i>	$\Delta C_{p0}$	$\Omega$	$q_{cavity}$	$q_{tip}$	$q_{side}$	$q_{total}$	$\Gamma$
18	-0.23517	<b>8.12%</b>	-26.64	-30.14	-11.09	-67.88	<b>-6.91%</b>
44	-0.23519	<b>8.11%</b>	-27.15	-30.11	-11.22	-68.48	<b>-5.94%</b>
47	-0.23519	<b>8.16%</b>	-27.24	-30.10	-11.22	-68.55	<b>-6.02%</b>

On the other hand, the effects of blowing ratio and casing relative motion on flow characteristics of the tip region are known. The best three cases with the lowest heat transfer at the tip region were selected to investigate the effects of blowing ratio and relative casing motion. These are cases 18, 44 and 47. These cases were run with a blowing ratio of 0.4 and a specific relative motion calculated from AFTRF parameters [47].

Table 5,6,7, and 8 shows the aerodynamic loss coefficient and heat transfer in the tip region of three cases with different parameters. The aerodynamic loss coefficient is directly affected by the addition of casing relative motion. It increases almost 8% for all three cases with high and low blowing ratios. On the other hand, the effect of the blowing ratio on the aerodynamic loss coefficient is not significant. In addition, heat transfer on the tip surface is another objective that is studied with different blowing ratios and the addition of casing relative motion. The magnitude of heat transfer on the tip region increases about 4-7% when the blowing rate is reduced to 0.4. On the other hand, casing relative motion significantly decreases the magnitude of heat transfer to the tip surface by about 9-12% with respect to the case without casing relative motion,, and its effect is more significant than the blowing ratio.



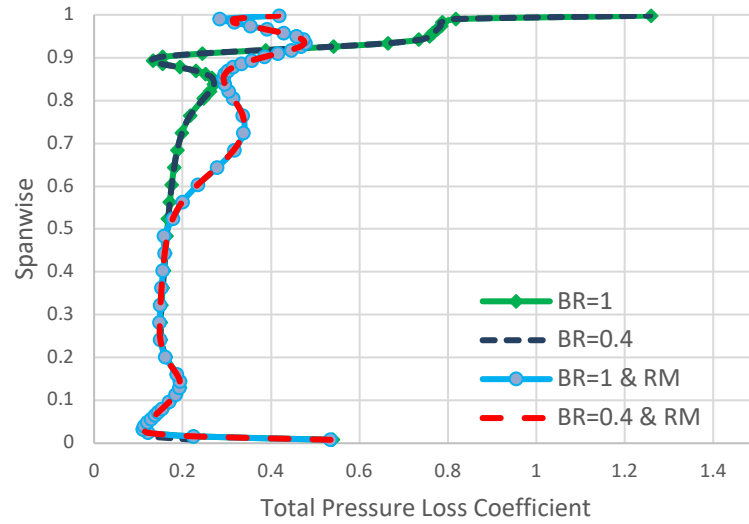


**Figure 16:** Spanwise distribution of the total pressure loss coefficient,  $0.47 C_x$ .

The distribution of the total pressure loss coefficient in the spanwise direction is shown in Figure 16 with high and low blowing ratios. Figure 16 also included with and without casing relative motion. It clearly shows that while the blowing ratio does not significantly affect aerodynamic loss, casing relative motion significantly changes it. With the addition of casing relative motion, the total pressure loss coefficient decreases in the region close to the casing. However, the total pressure loss coefficient increases in the region between midspan and 90% span.

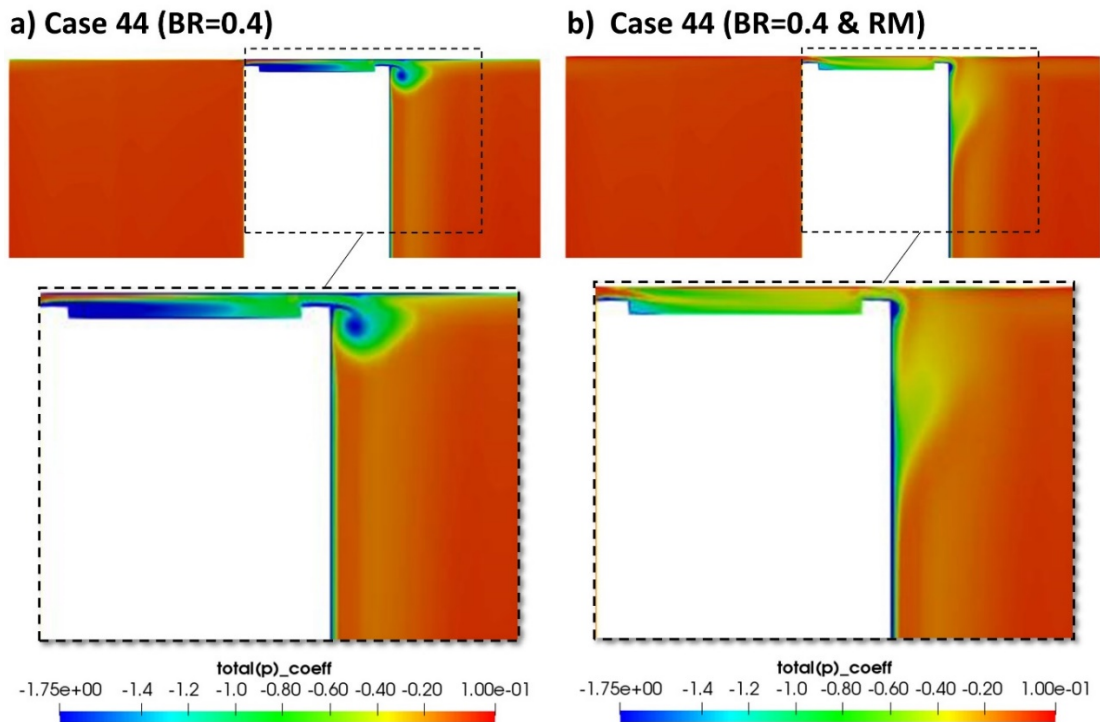
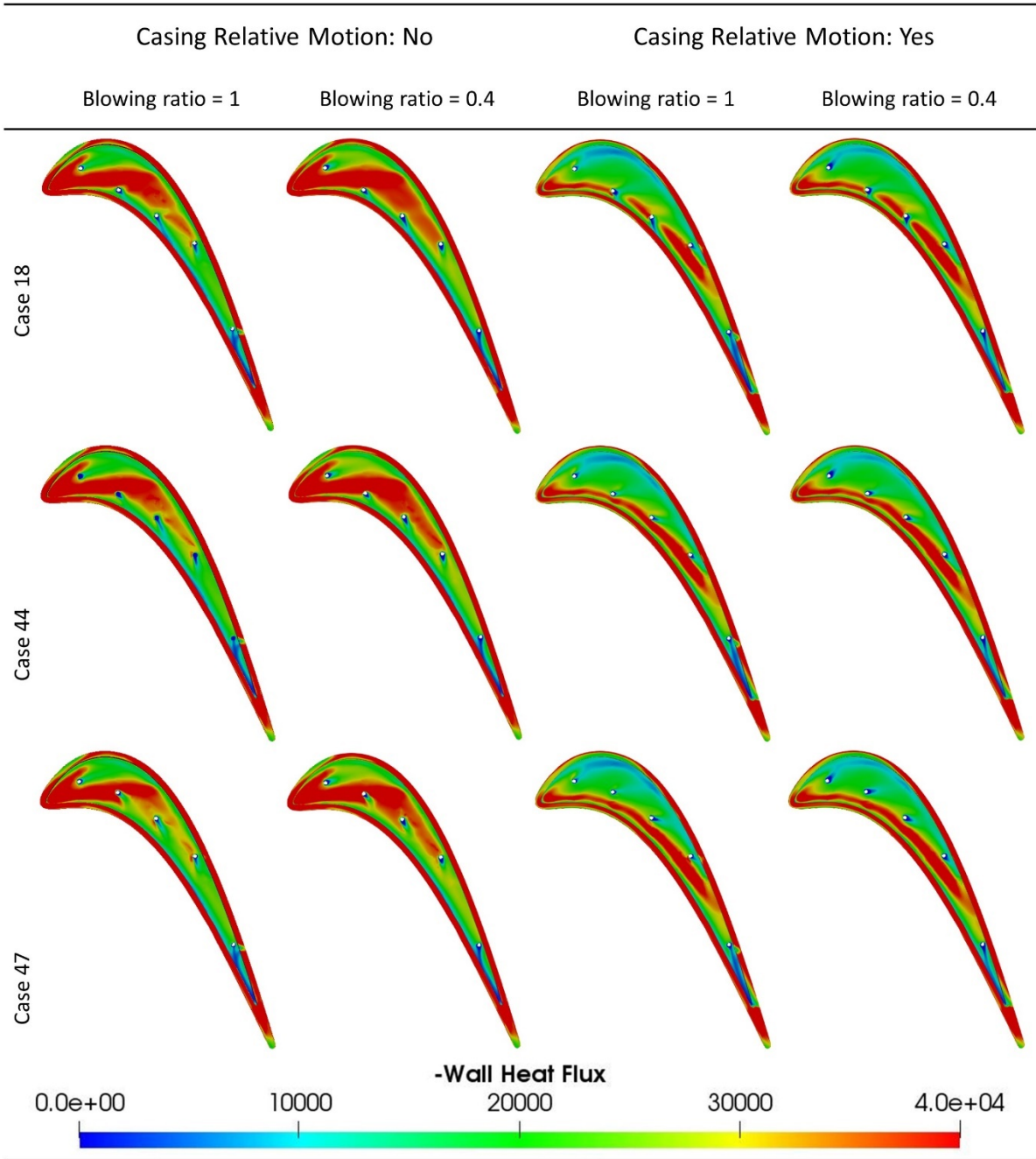


**Figure 17:** Total pressure coefficient on the section at  $0.47 C_x$ . a) Case 44 with low blowing ratio b) Case 44 with low blowing ratio and the addition of casing relative motion.

The total pressure coefficient on the section at  $0.47 C_x$  is shown in Figure 17. It clearly shows a similar structure when compared to Figure 16. With the addition of casing relative motion, the tip leakage vortex is compressed to the suction sidewall of the blade, however effect of the passage vortex increases. In the end, aerodynamic loss increases with the addition of casing relative motion.

**Table 9:** Absolute heat transfer rate on tip surface of different blowing ratios and casing relative motion cases.



In addition, the effect of casing relative motion and blowing ratio on tip surface heat transfer is noticeable, and Table 9 shows the comparison between different cases. The low blowing ratio slightly increases the magnitude of wall heat flux on the tip surface for all three cases with and without casing relative motion. On the

other hand, the effect of casing relative motion on tip surface heat transfer is higher than the blowing ratio. As mentioned above, casing relative motion pushes the leakage flow to the suction sidewall of the blade, and it decreases tip leakage flow. In the same way, it also compresses the leakage flow in the cavity to the pressure sidewall of the cavity. This also increases local total pressure near the pressure sidewall of the cavity surface, and this means less fluid enters the cavity region. As a result, heat transfer on the tip surface severely decreases. This is also obvious that more holes close to the pressure sidewall of the cavity would be better to decrease heat transfer on the tip surface. However, to find the best positions, an optimization study should be performed with the addition of casing relative motion.

## 5. Conclusions

This study numerically analyzes a turbine blade using a linear cascade model. The effects of film cooling and hole positions of film cooling on a squealer tip surface are investigated. Hole positions are optimized for total pressure loss coefficient and heat transfer rate on the tip surface. And also, the impact of blowing ratio and casing relative motion is studied. The significant findings are as follows:

- When Case 44, which has the lowest heat transfer to the tip surfaces in the optimization study, compared to the no-film-cooling case; heat transfer to the cavity, top and side surfaces of the squealer tip are reduced respectively by 18.9%, 8.9% and 13.1%, which is 13.4% reduction in total.
- There is a 15.7% difference in cavity surface heat transfer rate between the optimization study's highest (Case 34) and lowest (Case 44) heat transfer cases. The difference is 7.2% for the whole tip region.
- On the other hand, film cooling slightly increases the total pressure loss coefficient compared to the no-film-cooling case for all optimization cases. The increase is less than 1%. As a result, the second objective of the optimization study, the total pressure loss coefficient, may be neglected, considering its significant contribution to reducing heat transfer on the tip surface.
- While there is no significant impact of blowing ratio on the total pressure loss coefficient, the total pressure loss coefficient decreases by almost 8% with the impact of casing relative motion.
- On the other hand, the reduction in blowing ratio to 0.4 increases the magnitude of heat transfer on the tip region by 4-7%, while the addition of casing relative motion decreases it by about 9-12%. The impact of casing relative motion is more dominant than the impact of blowing ratio as far as the heat transfer on the tip

surface is concerned.

In order not to update the mesh every time the hole positions change, the cooling holes are defined as patches formed on the cavity surface via the topoSet and createPatch utilities of OpenFOAM®. Even though this approach led to not exactly circular holes and minimal deviations in the cooling airflow rate due to slight hole area variations, it allowed using the same mesh for all the CFD predictions obtained in this study. Considering the number of CFD solutions performed in this study, this approach provides considerable practicality.

In conclusion, the optimum positions of film cooling holes depend on the characteristics of tip leakage flow, and these positions changes with respect to the geometry and boundary conditions of the blade. Hence, the cooling effectiveness can be improved by employing a position optimization process to place the film cooling holes.

## References

- [1] Han, J. C., Dutta, S., & Ekkad, S. (2012). Gas turbine heat transfer and cooling technology. CRC press, ISBN 9781439855683.
- [2] Saha, A. K., Acharya, S., Bunker, R., & Prakash, C. (2006). Blade tip leakage flow and heat transfer with pressure-side winglet. *International Journal of Rotating Machinery*, 2006. doi:10.1155/IJRM/2006/17079.
- [3] Azad, G. S., Han, J. C., Bunker, R. S., & Lee, C. P. (2002). Effect of squealer geometry arrangement on a gas turbine blade tip heat transfer. *J. Heat Transfer*, 124(3), 452-459. doi:10.1115/1.1471523.
- [4] Acharya, S., Yang, H., Ekkad, S. V., Prakash, C., & Bunker, R. (2002, January). Numerical simulation of film cooling on the tip of a gas turbine blade. In *Turbo Expo: Power for Land, Sea, and Air* (Vol. 36088, pp. 1051-1062). doi:10.1115/gt2002-30553.
- [5] Key, N. L., & Arts, T. (2006). Comparison of turbine tip leakage flow for flat tip and squealer tip geometries at high-speed conditions. *Journal of Turbomachinery*, 128 (2) 213–220. doi:10.1115/1.2162183.
- [6] Schabowski, Z., Hodson, H., Giacche, D., Power, B., & Stokes, M. R. (2014). Aeromechanical optimization of a winglet-squealer tip for an axial turbine. *Journal of Turbomachinery*, 136(7), 071004. doi:10.1115/1.4025687.
- [7] Dey, D., & Camci, C. (2001, June). Aerodynamic tip desensitization of an axial turbine rotor using tip platform extensions. In *Turbo Expo: Power for Land, Sea, and Air* (Vol. 78507, p. V001T03A069). ASME. doi:10.1115/2001-GT-0484.
- [8] Ledezma, G. A., Allen, J., & Bunker, R. S. (2013, September). An experimental and numerical investigation into the effects of squealer blade tip modifications on aerodynamic performance. In *ASME Turbine Blade Tip Symposium* (Vol. 56079, p. V001T03A002). American Society of Mechanical Engineers. doi:10.1115/TBTS2013-2004.
- [9] Yan, X., Huang, Y., & He, K. (2017). Investigations into heat transfer and film cooling effect on a squealer-winglet blade tip. *International Journal of Heat and Mass Transfer*, 115, 955-978. doi:10.1016/j.ijheatmasstransfer.2017.08.090.
- [10] Du, K., Li, Z., Li, J., & Sunden, B. (2019). Influences of a multi-cavity tip on the blade tip and the over tip casing aerothermal performance in a high-pressure turbine cascade. *Applied Thermal Engineering*, 147, 347-360. doi:10.1016/j.applthermaleng.2018.10.093.

- [11] Jiang, S., Li, Z., & Li, J. (2019). Effects of the squealer winglet structures on the heat transfer characteristics and aerodynamic performance of turbine blade tip. *International Journal of Heat and Mass Transfer*, 139, 860-872. doi:10.1016/j.ijheatmasstransfer.2019.05.064.
- [12] Zhou, Z., Chen, S., Li, W., & Wang, S. (2019). Thermal performance of blade tip and casing coolant injection on a turbine blade with cavity and winglet-cavity tip. *International Journal of Heat and Mass Transfer*, 130, 585-602. doi:10.1016/j.ijheatmasstransfer.2018.10.130.
- [13] Wang, J., Sundén, B., Zeng, M., & Wang, Q. W. (2012). Influence of different rim widths and blowing ratios on film cooling characteristics for a blade tip. *Journal of heat transfer*, 134(6). doi:10.1115/1.4006017.
- [14] Sakaoglu, S., & Kahveci, H. S. (2019). Effect of cavity depth on thermal performance of a cooled blade tip under rotation. *International Journal of Heat and Mass Transfer*, 143, 118561. doi:10.1016/j.ijheatmasstransfer.2019.118561.
- [15] Eriksen, V. L., & Goldstein, R. J. (1974). Heat transfer and film cooling following injection through inclined circular tubes. *Journal of heat transfer*, 96(2): 239-245. doi:10.1115/1.3450171.
- [16] Yan, X., Huang, Y., & He, K. (2018). Effect of ejection angle and blowing ratio on heat transfer and film cooling effect on a winglet tip. *International Journal of Heat and Mass Transfer*, 125, 357-374. doi:10.1016/j.ijheatmasstransfer.2018.04.097.
- [17] Kim, Y. W., & Metzger, D. E. (1995). Heat transfer and effectiveness on film cooled turbine blade tip models. *Journal of Turbomachinery*, 117(1): 12-21. doi:10.1115/1.2835630.
- [18] Cho, H. H., & Goldstein, R. J. (1995). Heat (Mass) Transfer and Film Cooling Effectiveness with Injection Through Discrete Holes: Part II—On the Exposed Surface. *Journal of Turbomachinery*, 117(3): 451-460. doi:10.1115/1.2835681.
- [19] Rezasoltani, M., Lu, K., Schobeiri, M. T., & Han, J. C. (2015). A combined experimental and numerical study of the turbine blade tip film cooling effectiveness under rotation condition. *Journal of Turbomachinery*, 137(5), 051009. doi:10.1115/GT2014-25625.
- [20] Wang, J., Sundén, B., Zeng, M., & Wang, Q. (2015). Film cooling effects on the tip flow characteristics of a gas turbine blade. *Propulsion and Power Research*, 4(1), 9-22. doi:10.1016/j.jprr.2015.02.003.
- [21] Rao, N. M., & Camci, C. (2004, January). Axial turbine tip desensitization by injection from a tip trench: Part 2—leakage flow sensitivity to injection location. In *Turbo Expo: Power for Land, Sea, and Air* (Vol. 41707, pp. 1089-1098). doi:10.1115/GT2004-53258.
- [22] Cheng, F. N., Zhang, J. Z., Chang, H. P., & Zhang, J. Y. (2018). Investigations of film-cooling effectiveness on the squealer tip with various film-hole configurations in a linear cascade. *International Journal of Heat and Mass Transfer*, 117, 344-357. doi:10.1016/j.ijheatmasstransfer.2017.09.100.
- [23] Yang, H., Chen, H. C., & Han, J. C. (2004, January). Numerical prediction of film cooling and heat transfer with different film-hole arrangements on the plane and squealer tip of a gas turbine blade. In *Turbo Expo: Power for Land, Sea, and Air* (Vol. 41685, pp. 177-187). doi:10.1115/GT2004-53199.
- [24] Ahn, J., Mhetras, S., & Han, J. C. (2005). Film-cooling effectiveness on a gas turbine blade tip using pressure-sensitive paint. *J. Heat Transfer*, 127(5), 521-530. doi:10.1115/1.1909208.
- [25] He, K. (2017). Investigations of film cooling and heat transfer on a turbine blade squealer tip. *Applied Thermal Engineering*, 110, 630-647. doi:10.1016/j.applthermaleng.2016.08.173.
- [26] Park, J. S., Lee, D. H., Rhee, D. H., Kang, S. H., & Cho, H. H. (2014). Heat transfer and film cooling effectiveness on the squealer tip of a turbine blade. *Energy*, 72, 331-343. doi:10.1016/j.energy.2014.05.041.

- [27] Wang, Y., Song, Y., Yu, J., & Chen, F. (2019). Effect of the injection orientation and position on the leakage flow in a honeycomb-tip turbine cascade. *International Journal of Heat and Mass Transfer*, 144, 118633. doi:10.1016/j.ijheatmasstransfer.2019.118633.
- [28] Senel, C. B., Maral, H., Kavurmacioglu, L. A., & Camci, C. (2018). An aerothermal study of the influence of squealer width and height near a HP turbine blade. *International Journal of Heat and Mass Transfer*, 120, 18-32. doi:10.1016/j.ijheatmasstransfer.2017.12.017.
- [29] Yıldız, F. (2019). Position Optimization of Film Cooling Holes on a Squealer Turbine Blade Tip (Master's Thesis, Marmara University (Turkey)). 28243114.
- [30] Wilcox, D. C. (1993). Comparison of two-equation turbulence models for boundary layers with pressure gradient. *AIAA Journal*, 31(8), 1414-1421. doi:10.2514/3.11790.
- [31] Menter, F. R. (1994). Two-equation eddy-viscosity turbulence models for engineering applications. *AIAA Journal*, 32(8), 1598-1605. doi:10.2514/3.12149.
- [32] OpenFOAM®, <https://openfoam.org/>, accessed: 31-07-2021.
- [33] Đozić, D. J., & Urošević, B. D. G. (2019). Application of artificial neural networks for testing long-term energy policy targets. *Energy*, 174, 488-496. doi:10.1016/j.energy.2019.02.191.
- [34] Poort, J. P., Ramdin, M., van Kranendonk, J., & Vlugt, T. J. (2019). Solving vapor-liquid flash problems using artificial neural networks. *Fluid Phase Equilibria*, 490, 39-47. doi:10.1016/j.fluid.2019.02.023.
- [35] Taheri, M. H., Abbasi, M., & Jamei, M. K. (2019). Using artificial neural network for computing the development length of MHD channel flows. *Mechanics Research Communications*, 99, 8-14. doi:10.1016/j.mechrescom.2019.06.003.
- [36] Deveci, K., Maral, H., Senel, C. B., Alpman, E., Kavurmacioglu, L., & Camci, C. (2018). Aerothermal optimization of squealer geometry in axial flow turbines using genetic algorithm. *Journal of Thermal Engineering*, 4(3), 1896-1911.
- [37] Maral, H., Alpman, E., Kavurmacioglu, L., & Camci, C. (2019). A genetic algorithm based aerothermal optimization of tip carving for an axial turbine blade. *International Journal of Heat and Mass Transfer*, 143, 118419. doi:10.1016/j.ijheatmasstransfer.2019.07.069.
- [38] Maral, H., Şenel, C. B., Deveci, K., Alpman, E., Kavurmacioglu, L., & Camci, C. (2020). A genetic algorithm based multiobjective optimization of squealer tip geometry in axial flow turbines: a constant tip gap approach. *Journal of Fluids Engineering*, 142(2). doi:10.1115/1.4044721.
- [39] Octave, <https://www.gnu.org/software/octave/>, accessed: 22-01-2020.
- [40] Deb, K., Pratap, A., Agarwal, S., & Meyarivan, T. A. M. T. (2002). A fast and elitist multiobjective genetic algorithm: NSGA-II. *IEEE transactions on evolutionary computation*, 6(2), 182-197. doi:10.1109/4235.996017.
- [41] Camara, M. V. O., Ribeiro, G. M., & Tosta, M. D. C. R. (2018). A Pareto optimal study for the multiobjective oil platform location problem with NSGA-II. *Journal of Petroleum Science and Engineering*, 169, 258-268. doi:10.1016/j.petrol.2018.05.037.
- [42] Han, H., Yu, R., Li, B., & Zhang, Y. (2019). Multiobjective optimization of corrugated tube inserted with multi-channel twisted tape using RSM and NSGA-II. *Applied Thermal Engineering*, 159, 113731. doi:10.1016/j.applthermaleng.2019.113731.
- [43] Vo-Duy, T., Duong-Gia, D., Ho-Huu, V., Vu-Do, H. C., & Nguyen-Thoi, T. (2017). Multiobjective optimization of laminated composite beam structures using NSGA-II algorithm. *Composite Structures*, 168, 498-509. doi:10.1016/j.compstruct.2017.02.038.
- [44] Camci, C. (2004). A turbine research facility to study tip desensitization including cooling flows. *VKI Lecture Series on "Turbine Blade Tip Design and Tip Clearance Treatment"*, 1-26. ISBN 2-930389-51-6, Brussels, Belgium.

- [45] Turgut, Ö. H., & Camci, C. (2016). Factors influencing computational predictability of aerodynamic losses in a turbine nozzle guide vane flow. *Journal of Fluids Engineering*, 138(5). doi:10.1115/1.4031879.
- [46] McLean, C., Camci, C., & Glezer, B. (2001). Mainstream Aerodynamic Effects Due to Wheelspace Coolant Injection in a High-Pressure Turbine Stage: Part I—Aerodynamic Measurements in the Stationary Frame. *J. Turbomach.*, 123(4), 687-696. doi:10.1115/1.1401026.
- [47] Beer, W. (2008). Optimisation of a compound lean turbine blade in a linear cascade. (Doctoral dissertation, Technischen Universität Wien (Austria)).
- [48] Klaput, T. (1996). Control of Near Wall Flow on an Isolated Airfoil at High Angle of Attack Using Piezoelectric Surface Vibration Elements. (Master's Thesis, Penn State (USA)).
- [49] Somers, D. M., & Maughmer, M. D. (1990). The SM701 Airfoil. Airfoils, Inc., December.
- [50] Somers, D., & Maughmer, M. D. (1992). THE SM701 airfoil: an airfoil for world-class sailplanes. *Technical Soaring*, 16(3), 70-77.
- [51] Langtry, R. B., & Menter, F. R. (2009). Correlation-based transition modeling for unstructured parallelized computational fluid dynamics codes. *AIAA journal*, 47(12), 2894-2906. doi:10.2514/1.42362.
- [52] Helton, J. C., & Davis, F. J. (2003). Latin hypercube sampling and the propagation of uncertainty in analyses of complex systems. *Reliability Engineering & System Safety*, 81(1), 23-69. doi:10.1016/S0951-8320(03)00058-9.

**Appendix – I:** Coordinates of tip airfoil section of AFTRF at Penn State [44]

x-Coordinate [mm]	y-Coordinate [mm]	x-Coordinate [mm]	y-Coordinate [mm]
-1.512	1.906	29.33	-23.823
-4.31	4.462	30.965	-28.265
-7.173	6.741	32.506	-32.569
-10.096	8.716	33.952	-36.731
-13.076	10.349	35.318	-40.749
-16.089	11.609	36.606	-44.62
-19.099	12.49	37.823	-48.344
-22.058	13.015	38.971	-51.919
-24.794	13.232	40.005	-55.187
-27.277	13.263	40.931	-58.146
-29.497	13.188	41.752	-60.797
-31.452	13.056	42.47	-63.137
-33.145	12.919	43.089	-65.167
-34.58	12.833	43.61	-66.885
-35.808	12.826	44.053	-68.353
-36.838	12.905	44.43	-69.587
-37.673	13.059	44.744	-70.605
-38.322	13.261	44.968	-71.42
-38.792	13.489	45.062	-72.063
-39.115	13.711	44.966	-72.539
-39.358	13.93	44.739	-72.878
-39.526	14.13	44.492	-73.091
-39.637	14.292	44.274	-73.203
-39.752	14.508	44.086	-73.258
-39.869	14.813	43.827	-73.292
-39.953	15.212	43.503	-73.251
-39.982	15.701	43.16	-73.102
-39.921	16.351	42.808	-72.725
-39.721	17.175	42.452	-72.129
-39.355	18.171	42.085	-71.364
-38.784	19.327	41.697	-70.593
-38.004	20.649	41.105	-69.326
-36.987	22.128	40.48	-68.032
-35.701	23.816	39.741	-66.503
-34.102	25.67	38.886	-64.739
-32.14	27.632	37.915	-62.741
-29.729	29.584	36.828	-60.509
-26.81	31.38	35.617	-58.044
-23.339	32.808	34.294	-55.348
-19.512	33.645	32.901	-52.538
-15.434	33.811	31.44	-49.616
-11.229	33.241	29.908	-46.584
-7.031	31.901	28.301	-43.443
-2.982	29.781	26.616	-40.196
0.816	26.956	24.845	-36.845
4.341	23.558	22.986	-33.394
7.508	19.823	21.092	-29.692
10.379	15.856	19.159	-26.552
13.025	11.736	17.176	-23.17
15.479	7.499	15.139	-19.889
17.772	3.172	13.038	-16.508
19.925	-1.226	10.878	-13.241
21.923	-5.674	8.623	-10.034
23.922	-10.166	6.276	-6.894
25.791	-14.692	3.813	-3.844
27.59	-19.246	1.224	-0.9



**Appendix – II: Coordinates of SM701 Airfoil [49], [50]**

Upper Surface		Lower Surface	
x/c	y/c	x/c	y/c
0.00168	0.00771	0.00016	-0.0021
0.00736	0.0191	0.00435	-0.0098
0.01701	0.03121	0.01501	-0.0163
0.03055	0.04344	0.03127	-0.0224
0.04794	0.05534	0.05277	-0.028
0.06915	0.06648	0.07923	-0.0329
0.09417	0.07658	0.11036	-0.0373
0.12295	0.08544	0.14575	-0.041
0.15541	0.09296	0.18488	-0.0442
0.19133	0.09914	0.22722	-0.0467
0.23041	0.10397	0.27222	-0.0485
0.27229	0.10746	0.31929	-0.0494
0.31654	0.10964	0.36784	-0.0494
0.36268	0.11055	0.41726	-0.048
0.41019	0.11018	0.46727	-0.0449
0.45853	0.10853	0.51811	-0.0398
0.50714	0.10557	0.56979	-0.0334
0.55548	0.1012	0.62191	-0.0262
0.60323	0.09517	0.67386	-0.0189
0.65041	0.0876	0.72497	-0.0118
0.69676	0.07903	0.77446	-0.0055
0.74171	0.0699	0.82144	-0.0004
0.78466	0.06055	0.86497	0.00324
0.82498	0.05125	0.90406	0.00526
0.86207	0.04221	0.93768	0.00567
0.89529	0.03348	0.96489	0.00463
0.92431	0.02493	0.98462	0.00262
0.94922	0.01669	0.99624	0.00073
0.96999	0.00946	1	0
0.98605	0.00405		
0.9964	0.00095		
1	0		